

Resolving Structural Avalanches in Amorphous Carbon with Arclength Continuation

Fraser Birks,^{1,*} Ibrahim Ghanem,² Lars Pastewka,² James Kermode,¹ and Maciej Buze³

¹*School of Engineering, University of Warwick, UK*

²*Faculty of Engineering, University of Freiburg, Germany*

³*School of Mathematical Sciences, University of Lancaster, UK*

(Dated: February 2, 2026)

Plastic deformation in amorphous solids is carried by localized shear transformations that self-organize into avalanches. In amorphous carbon modeled with a machine-learned interatomic potential, we find that the energetics and organization of these avalanches can be resolved by systematically following the underlying energy landscape. With a pseudo-arclength numerical continuation framework, we decompose avalanches into constituent shear transformations and determine their strain-dependent energetics. Our analysis shows that, prior to onset, avalanches have a latent structure that consists of well-separated local minima. We further demonstrate that arclength continuation yields an event driven framework for following avalanche dynamics, eliminating time-step effects on statistical avalanche properties such as distributions of stress drops.

During plastic deformation, materials undergo irreversible changes in their structure. In crystalline solids, the mechanism underlying this irreversibility is well established: it is the glide of dislocations, line defects whose motion results in the net sliding of planes of atoms [1]. In contrast, glassy materials, which lack long-range structural order, deform plastically through the localized yielding of small regions within the amorphous structure [2, 3]. These “soft” regions, referred to as shear transformation zones (STZs), typically consist of a few tens of atoms that undergo highly non-affine rearrangements [4].

Extensive research has been devoted to understanding the fundamental nature of STZs and determining whether there are structural indicators that can reliably predict their emergence [5]. A major challenge in this endeavor lies in the fact that STZs are not isolated entities, they interact through long-range elastic fields [6]. As a result, the activation of a single STZ can trigger the yielding of nearby regions, potentially leading to a cascade of correlated events, or structural avalanches [7]. Avalanches are most pronounced at low temperature and are often studied in athermal and quasi-static (AQS) simulations [8]. The phenomenology of systems at finite-temperature and finite rate is similar, with temperature and rate cutting off the observable avalanche sizes at small and large scales, respectively [9–12].

AQS uses sequences of finite-strain increments together with searches for the next local minimum to trace out the most likely low-temperature path of the driven system within its potential energy landscape. Fig. 1 demonstrates the AQS method for computing a stress-strain curve for the simple shear of a 4096 atom sample of amorphous carbon (a-C, density 2.7 g cm^{-3}), generated via a rapid liquid quench of carbon from 10,000 K at a rate of 1000 K/ps. For interatomic interactions, we used the realistic machine-learned atomic cluster expansion (ACE) potential from Qamar et al. [13, 14]. The stress-strain curve is shown in figure Fig. 1b. Discontinuous stress

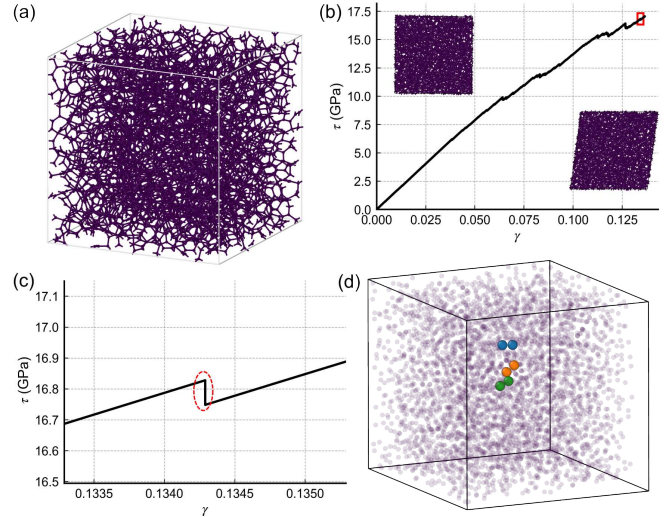


FIG. 1. Structure and plastic events in amorphous carbon. (a) A 4096-atom structure of amorphous carbon with a density of 2.7 g cm^{-3} . (b) The shear-stress shear-strain curve of the amorphous carbon structure. Note that γ is the simple shear strain. (c) An enlargement of the stress-strain curve corresponding to the position of the red box in (b). The stress drop encircled corresponds to a three-bond structural avalanche plastic event. (d) The 3-bond structural avalanche highlighted in (c). The three bonds involved are colored blue, orange and green.

drops that can be seen on this curve correspond to the activation of plastic events. Due to the covalent nature of bonding in a-C, plastic events necessarily involve the breaking and/or formation of bonds [15]. While some stress drops are associated with a single bond rearrangement, the majority are structural avalanches involving multiple bonds. One such example is the three-bond structural avalanche highlighted in Figs. 1c and d.

Two properties of AQS limit its usefulness in the study of avalanche events: (i) The finite step size makes it difficult to determine whether events are truly correlated, or

just occurring at strain values too close to resolve, and (ii) AQS simulations give no information about the inherent energetics of an avalanche, other than the trivial fact that the first barrier is zero at the instant of onset.

One way of overcoming shortcoming (ii) is to identify two mechanically stable configurations at the same applied strain before and after instability onset, and perform a nudged elastic band (NEB) [16, 17] calculation to determine the minimum energy path. This approach was employed in Ref. [18] to compute the energy barriers associated with instabilities for both single shear transformations and avalanches.

We have found that while using NEB directly can work for small avalanches with fewer than three bonds involved, it is completely unsuitable for larger avalanches. There are three reasons for this: (i) Many images (often > 150) are required to adequately resolve energy landscapes containing multiple intermediate minima and barriers of different sizes. (ii) Convergence frequently fails when near the avalanche onset strain. (iii) The energy pathway determined (the ordering of events) is highly sensitive to the initial guess. For further detail, see section A of the Supplementary Material.

In this Letter, we introduce a numerical tailored arclength continuation (AC) method which overcomes the limitations of both AQS and NEB simulations. With this method, we remove step-size dependence and show that avalanches would happen in an AQS simulation even with an infinitesimally small strain step. We reveal that at strains below onset, avalanches in amorphous carbon modeled with a realistic potential decompose into latent structures comprising chains of well separated local minima connected by index-1 saddle points. Going further, with minimal effort, we obtain full energetic information between the intermediate basins and saddle points of the latent structure at a range of strains. Once these are identified, we validate our results by running NEB calculations between adjacent intermediate states.

AC is a method for tracking continuous solution branches of non-linear equations as a control parameter varies [19]. In the context of amorphous plasticity, we are interested in finding sets of atomic positions $\mathbf{R} \in \mathbb{R}^{3N}$ (where N is the number of atoms) that correspond to energy minima or saddle points of a system, where all atomic forces vanish $\mathbf{F}(\mathbf{R}, \gamma) = \mathbf{0}$ simultaneously, as the applied strain γ changes. The key idea of AC is to parameterize the solution path $\{(\mathbf{R}(s), \gamma(s))\}_s$ using an arclength parameter s . In the AQS approach, the solution path $\{(\mathbf{R}(\gamma), \gamma)\}_\gamma$ is always parameterized by the applied strain, leading to singularities at bifurcation points, which are the critical values of the applied strain where STZs activate. In contrast, the AC approach allows a seamless traversal of the bifurcation points, meaning it is able to transition smoothly from minima to saddle (provided the interatomic potential is twice continuously differentiable in the vicinity of the bifurcation point, as is

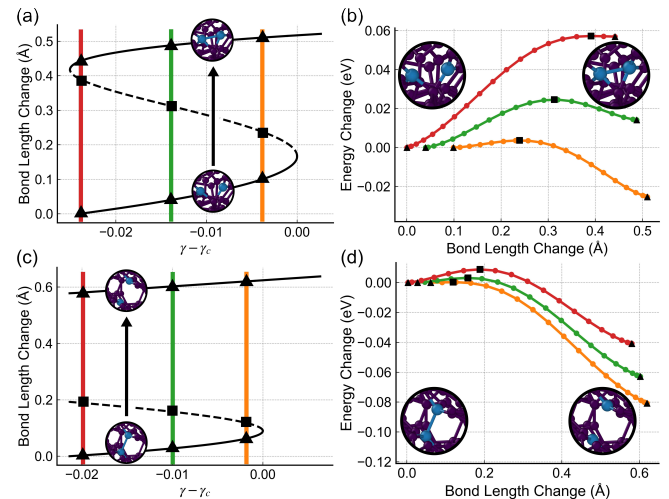


FIG. 2. The strain-dependent energy landscape of single-bond plastic events is explored using AC. (a) For a reversible event, the continuation curve follows the minimum associated with the open bond (lower branch, solid black) until the critical strain γ_c , where the barrier vanishes. AC then passes through the bifurcation to the central branch, corresponding to the index-1 saddle traced as strain decreases (dashed black), before reaching the upper branch associated with the formed bond (solid black). (b) Nudged elastic band (NEB) energy profiles sampled across this landscape, with color-coded strains indicated in (a), show excellent agreement between NEB and continuation saddle energies (triangles and squares denote minima and saddles). (c)–(d) The same analysis for an irreversible event shows no continuous path from the central to the upper branch, consistent with the strongly asymmetric barrier revealed by the NEB profiles.

expected for any reasonable interatomic potential). The framework also admits a natural adaptive step size in s , which avoids the fixed step-size compromise inherent to AQS simulations and ensures that bifurcation events along the solution path are not missed.

One limitation of typical AC which proves problematic in this application is the requirement for second derivative (Hessian) information. For atomistic systems, routes toward computing the Hessian are either numerical or analytical, which are both prohibitively computationally expensive for realistic interatomic potentials such as the ACE potential employed here. We therefore apply a Hessian-free pseudo-arclength numerical continuation algorithm similar to that previously applied to atomistic systems by Buze & Kermode [20], with full algorithmic details presented in section B of the Supplementary Material. AC-based approaches in atomistic modeling have also previously been explored in Refs. [21, 22] to study brittle fracture and in Ref. [23] to study response of an FCC nanoslab of nickel to loading. Ref. [24] also presents a related idea, the use of implicit differentiation to explore atomistic energy landscapes via a Hessian-free approximation.

We first validated this method through application to single-bond plastic events. Fig. 2a shows the path traversed by the continuation method for a reversible event in which a single bond forms. The path has three branches. The first (lower) branch, represents an open bond, with the rightmost point corresponding to the strain at which the bond would naturally form in a quasi-static simulation. After the first bifurcation point, the central branch (dashed line), where strain values retreat, represents the set of saddle points which lie between the two stable branches. Finally, after the second bifurcation point, the system re-enters a minimum, with increasing strain corresponding to the further closing of the two (now bonded) atoms. Three nudged-elastic-band (NEB) calculations across this bifurcation diagram are shown in Fig. 2b. The strain value of each NEB corresponds to the vertical line of matching color across Fig. 2a. The energies from the continuation branch minima are marked as triangles, while the saddle energies predicted by the continuation are marked as squares.

Fig. 2c and d demonstrate how this technique can be applied to an event where the breaking of individual bonds is not reversible upon strain removal — i.e., where there is not a single continuous path connecting stable segments. The initial procedure is the same, but rather than traversing the full curve with continuation directly, a relaxation is carried out from the saddle into the adjacent minima, effectively ‘jumping’ the gap. By inspecting the energy landscape in Fig. 2d it is clear why such a gap exists — the energy barrier associated with the event is greatly asymmetrical, and remains similarly asymmetrical for a range of strains. In both the reversible and irreversible cases, the agreement between the NEB and continuation saddle energies is excellent.

We now turn to the complex case of traversing a multi-event avalanche with AC. For visualization, we define a reaction coordinate, the cumulative active bond-length change μ , defined as $\sqrt{\sum_{ij} (r_{ij} - r_{ij}^0)^2}$, where r and r^0 refer to bond lengths in the deformed and a reference structure respectively and the sum runs over the ‘active’ bonds between pairs of atoms i, j (all bonds involved in the avalanche event). Avalanche exploration proceeds through a controlled sequence of continuation and relaxation steps. As in the irreversible single-bond case, we first run continuation through the initial bifurcation point to the first saddle. Biased relaxations are performed from the saddle into the adjacent basins. Near the avalanche onset strain, the system undergoes the full cascade, but at lower strains the system lands in intermediate basins corresponding to triggering only a subset of events. For the six-bond avalanche explored in Fig. 3a, the relaxing from the first saddle (blue dashed line) to the adjacent minima (lower orange solid line) corresponds to the triggering of only a single event. By iterating this procedure — starting from each newly discovered basin

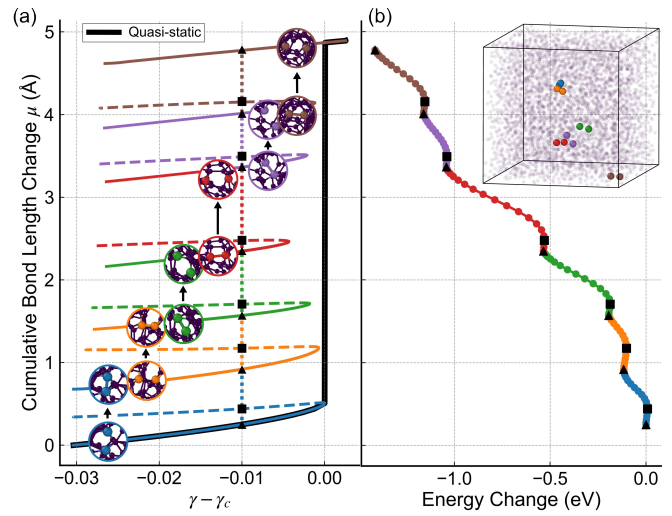


FIG. 3. The strain-dependent energy landscape of a six-bond avalanche. (a) A set of continuation curves reveals the latent structure of the avalanche. The AQS trajectory (thick black line) triggers the full avalanche at the critical strain γ_c . In contrast, AC can traverse the bifurcation at γ_c onto the index-1 saddle associated with the first bond-breaking event (dashed blue). Relaxation from this saddle at lower strain leads to an intermediate basin in which a single bond has broken (orange), and repeating this procedure (green, red, purple, and brown) resolves the avalanche into successive events. All intermediate basins disappear below γ_c , implying that even an infinitesimal-step AQS protocol would still trigger the full avalanche. (b) A nudged elastic band (NEB) energy landscape at $\gamma_{xy} - \gamma_c = -0.01$, assembled from sequential NEBs between adjacent intermediate basins, with continuation minima and saddles marked by triangles and squares. The NEB and continuation saddle energies agree closely. Insets in (a) and (b) indicate the ordering of events and the full avalanche.

and using continuation to traverse the next saddle — we can reconstruct the avalanche as a chain of discrete transitions. In Fig. 3a, the six-event avalanche has been dissected into six unique single-bond events, colored blue, orange, green, red, purple and brown. A full energy profile across these events formed from individual NEBs between each adjacent intermediate basin at a strain 0.01 below the onset strain γ_c is shown in Fig. 3b. For all transitions, the continuation barrier energies agree perfectly with those predicted by each NEB calculation.

In general, we observe that avalanches cannot always be split perfectly into sequences of single bond events; it is common for single-bond events to be so correlated that they do not disentangle even at lower strains. The range of avalanche sizes examined, together with a discussion of their degree of separability and algorithmic limitations is provided in section C of the Supplementary Material.

Our observations highlight three interesting features of avalanches in amorphous carbon: (i) avalanches are formed from distinct sequences of low-dimensional events, (ii) these events are highly separable at strains

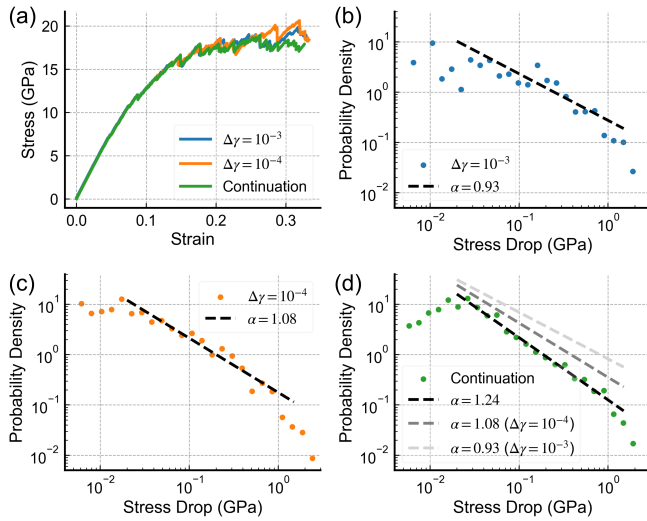


FIG. 4. A comparison between AQS and continuation simulations is shown. (a) Overlaid stress-strain curves from AQS simulations with step sizes $\Delta\gamma = 10^{-3}$ (blue) and 10^{-4} (orange), together with continuation results (green). The curves diverge upon entering the plastic flow regime ($\gamma \gtrsim 0.17$). (b-d) Log-log plots of the binned probability density of stress drops for $\gamma > 0.17$ over 5 repeats. AQS results are shown for $\Delta\gamma = 10^{-3}$ in (b) and $\Delta\gamma = 10^{-4}$ in (c); in both cases, finite step size leads to an underestimation of the fitted power-law exponent (dashed black). In contrast, the continuation algorithm in (d) eliminates step-size dependence, yielding a steeper and more clearly defined power-law scaling.

below avalanche onset and (iii) the sequence displays a robust internal latent structure in which the constituent events are connected by a unique chain of local minima and index-1 saddle points. Crucially, this structure only appears below the avalanche onset strain, meaning even an infinitesimal quasi-static strain step taken at the critical strain of the first event would trigger the entire avalanche.

Going further, Fig. 4 demonstrates that continuation can not only resolve individual avalanche structures, but also yields a framework for event-driven simulation of avalanche dynamics. Panel (a) compares stress-strain curves obtained from AQS simulations with two different strain increments to the continuation result. While all curves coincide in the elastic regime, they begin to diverge upon entering steady plastic flow ($\gamma \gtrsim 0.17$), reflecting the accumulation of step-size-dependent errors in AQS. Panels (b) and (c) show the corresponding stress-drop distributions measured from a number of AQS trajectories in the plastic flow regime at $\Delta\gamma = 10^{-3}$ and 10^{-4} , respectively. In both cases, the finite strain increment causes multiple nearby instabilities to be triggered within a single step, merging distinct plastic events and suppressing small stress drops. This manifests as a systematic flattening of the distribution and an apparent reduction of the fitted power-law exponent, which per-

sists even as the step size is reduced. By contrast, panel (d) shows the distribution obtained from AC, where individual bifurcations are resolved directly. The resulting stress-drop statistics are independent of strain step size and exhibit a steeper, more clearly defined power-law scaling, indicating that continuation provides direct access to the intrinsic avalanche statistics underlying plastic flow.

The ability to traverse complex regions of the energy landscape for a system modeled with a high-fidelity machine-learned potential suggests that this framework is well suited to interrogate the microscopic physics of plasticity in realistic amorphous systems. In particular, the readily attainable energetics opens the way to directly measuring how energy barriers in the system are altered by nearby plastic events; information that could be used to build accurate coarse-grained elasto-plastic models or derive statistical relationships. Applying AC methods to avalanches in other glassy systems is a natural avenue for future work. Earlier studies—both in simple Lennard-Jones glasses [25–28] and in metallic glasses using embedded-atom potentials [29] could have benefited from this approach.

Beyond these directions, the approach also has clear potential for studying more complex phenomena in amorphous carbon, including fracture processes and the emergence of shear bands, where detailed knowledge of the underlying energy landscape could prove especially informative. It would also be valuable to relate the ordering of events identified within an avalanche’s latent structure to that obtained from established avalanche discretization methods, such as overdamped dynamics [30, 31]. Our preliminary analysis (see Supplementary Material, Section D) indicates that although the two orderings are correlated, the dynamical causal chain does not always coincide exactly with the event ordering inferred from the latent structure.

In summary, we have introduced an arclength continuation-based method and applied it to investigate plastic events in amorphous carbon modeled with a machine-learned ACE potential. Unlike traditional approaches combining AQS and NEB simulations, AC is guaranteed to find bifurcation points and can directly traverse saddle points, allowing the extraction of energy barriers for each plastic event. For this realistic system, we showed that at strains below onset, avalanches can be decomposed into latent structures comprising chains of well-separated local minima connected by index-1 saddle points, the energetics of which were validated separately using NEB calculations between intermediate basins. In future, we believe that AC will be a crucial tool in the investigation of avalanches in atomistic systems, and that elucidating avalanche latent structures will allow for a clearer mapping between individual rearrangements, their mutual interactions, and the collective mechanical behavior that emerges at larger scales.

Acknowledgements — We are grateful to Matous Mrovec for sharing an early version of the a-C potential published in Ref. [13], and to Albert P. Bartók for helpful discussions. FB is supported by a studentship from the UK Engineering and Physical Sciences Research Council–funded Centre for Doctoral Training in Modelling of Heterogeneous Systems (Grant No. EP/S022848/1). This work was partially funded by the German Research Foundation (DFG) through Research Unit 5099 (Project 431945604). We acknowledge the University of Warwick Scientific Computing Research Technology Platform for computational support. Additional computations were carried out on bwForCluster NEMO2 (State of Baden-Württemberg and DFG Project 455622343), with further resources provided by Sovereign AI and Isambard-AI. MB is supported by Research England under the Expanding Excellence in England (E3) funding stream, which was awarded to MARS: Mathematics for AI in Real-world Systems in the School of Mathematical Sciences at Lancaster University. Part of this research was performed while MB was a visiting fellow at the Institute for Pure and Applied Mathematics (IPAM), as part of the long program New Mathematics for the Exascale: Applications to Materials Science. IPAM is supported by the U.S. National Science Foundation (Grant No. DMS-1925919).

Data Availability Statement — The scripts and data generated for this study are available on Zenodo [32]. The arclength continuation algorithms used in this work are implemented in LACT, a Python–based LAMMPS [33] wrapper, which can be found on GitHub [34].

(2009).

- [10] S. Karmakar, E. Lerner, I. Procaccia, and J. Zylberg, Phys. Rev. E **82**, 031301 (2010).
- [11] C. Liu, E. E. Ferrero, F. Puosi, J. Barrat, and K. Martens, Phys. Rev. Lett. **116**, 065501 (2016).
- [12] D. Korchinski and J. Rottler, Phys. Rev. E **106**, 034103 (2022).
- [13] M. Qamar, M. Mrovec, Y. Lysogorskiy, A. Bochkarev, and R. Drautz, J. Chem. Theory Comput. **19**, 5151 (2023).
- [14] Note that a pre-released version of this potential was used to avoid a known problem with numerical instabilities affecting relaxations due to the explicit pairwise dispersion correction added to the published potential.
- [15] T. Kunze, M. Posselt, S. Gemming, G. Seifert, A. R. Konicek, R. W. Carpick, L. Pastewka, and M. Moseler, Tribology Letters **53**, 119–126 (2014).
- [16] G. Henkelman, B. P. Uberuaga, and H. Jónsson, J. Chem. Phys. **113**, 9901 (2000).
- [17] G. Henkelman and H. Jónsson, J. Chem. Phys. **113**, 9978 (2000).
- [18] F. Boioli, T. Albaret, and D. Rodney, Phys. Rev. E **95**, 033005 (2017).
- [19] E. L. Allgower and K. Georg, *Introduction to numerical continuation methods* (SIAM, 2003).
- [20] M. Buze and J. R. Kermode, Phys. Rev. E **103**, 033002 (2021).
- [21] X. Li, Eur. Phys. J. B **86**, 258 (2013).
- [22] M. Buze, T. Hudson, and C. Ortner, ESAIM: Mathematical Modelling and Numerical Analysis **54**, 1821 (2020).
- [23] S. Pattamatta, R. S. Elliott, and E. B. Tadmor, Proc. Natl. Acad. Sci. U.S.A. **111**, E1678 (2014).
- [24] I. Maliyov, P. Grigorev, and T. D. Swinburne, npj Comput. Mater. **11**, 22 (2025).
- [25] K. M. Salerno, C. E. Maloney, and M. O. Robbins, Phys. Rev. Lett. **109**, 105703 (2012).
- [26] A. Moriel, D. Richard, E. Lerner, and E. Bouchbinder, Phys. Rev. Res. **6**, 023167 (2024).
- [27] N. Oyama, T. Kawasaki, K. Kim, and H. Mizuno, Phys. Rev. Lett. **132**, 148201 (2024).
- [28] U. A. Dattani, S. Karmakar, and P. Chaudhuri, Phys. Rev. E **106**, 055004 (2022).
- [29] J. Duan, Y. J. Wang, L. H. Dai, and M. Q. Jiang, Phys. Rev. Mater. **7**, 013601 (2023).
- [30] O. U. Salman and L. Truskinovsky, Phys. Rev. Lett. **106**, 175503 (2011).
- [31] R. Baggio, O. U. Salman, and L. Truskinovsky, Phys. Rev. E **107**, 025004 (2023).
- [32] F. Birks, I. Ghanem, L. Pastewka, J. Kermode, and M. Buze, 10.5281/zenodo.18393712 (2026).
- [33] A. P. Thompson, H. M. Aktulga, R. Berger, D. S. Bolintineanu, W. M. Brown, P. S. Crozier, P. J. in 't Veld, A. Kohlmeyer, S. G. Moore, T. D. Nguyen, R. Shan, M. J. Stevens, J. Tranchida, C. Trott, and S. J. Plimpton, Comput. Phys. Commun. **271**, 108171 (2022).
- [34] M. Buze and F. Birks, LACT (LAMMPS Continuation Techniques), <https://github.com/mbuze/LACT>.

* fraser.birks@warwick.ac.uk

- [1] J. P. Hirth, J. Lothe, and T. Mura, J. Appl. Mech. **50**, 476 (1983).
- [2] A. S. Argon, Acta Metal. **27**, 47 (1979).
- [3] F. Spaepen, Acta Metal. **25**, 407 (1977).
- [4] M. L. Falk and J. S. Langer, Phys. Rev. E **57**, 7192 (1998).
- [5] D. Richard, M. Ozawa, S. Patinet, E. Stanifer, B. Shang, S. A. Ridout, B. Xu, G. Zhang, P. K. Morse, J.-L. Barrat, L. Berthier, M. L. Falk, P. Guan, A. J. Liu, K. Martens, S. Sastry, D. Vandembroucq, E. Lerner, and M. L. Manning, Phys. Rev. Mater. **4**, 113609 (2020).
- [6] C. Maloney and A. Lemaître, Phys. Rev. Lett. **93**, 016001 (2004).
- [7] J. P. Sethna, K. A. Dahmen, and C. R. Myers, Nature **410**, 242 (2001).
- [8] C. E. Maloney and A. Lemaître, Phys. Rev. E **74**, 016118 (2006).
- [9] A. Lemaître and C. Caroli, Phys. Rev. Lett. **103**, 065501

SUPPLEMENTARY MATERIAL A

NON-UNIQUENESS OF MINIMUM ENERGY PATHS IN NUDGED ELASTIC BAND SIMULATIONS

In amorphous solids under athermal quasi-static shear, a plastic event occurs when a local minimum of the potential-energy surface (PES) loses stability through a saddle-node bifurcation, in which the minimum collides with a nearby saddle, triggering a transition into a neighboring basin along the minimum-energy path (MEP) [1, 2]. To compute the MEP associated with a given plastic event, we use the Nudged Elastic Band (NEB) method [3, 4] following the procedure of Rodney and co-workers [5]. Immediately after an instability is detected, the shear direction is reversed to recover two stable configurations at the same applied strain—just before and just after the event—which serve as the fixed endpoints for the subsequent NEB calculation. Here we show that, for an avalanche comprising a sequence of bond transformations, the MEP between the same endpoints is not unique. The NEB solution is highly sensitive to how the initial images are constructed, and straightforward linear interpolation does not necessarily recover the dynamically realized pathway at the instability.

We analyze an avalanche comprising three bond-breaking events. As NEB endpoints, we select the configurations immediately before and after the avalanche at strain offsets $\gamma - \gamma_c = -0.03$, -0.02 , and -0.01 , where γ denotes the imposed shear strain and γ_c is the critical strain at which the instability occurs. We show zoomed views of the atomic configurations at $\gamma - \gamma_c = -0.03$ in Fig. 1a and b, with the displacement field between them overlaid on panel b. The atoms involved in the 3-bond transformations are highlighted in distinct colors. Instead of linearly interpolating the displacement field between the two configurations, we adopt a nonlinear interpolation scheme that biases the initial MEP guess toward one of the highlighted bonds. We construct N initial images by prescribing a per-atom power-law progression of the displacement along the path

$$\mathbf{D}_j^i = (\mathbf{R}_j^N - \mathbf{R}_j^1) \left(\frac{i}{N} \right)^{\alpha_j}, \quad (1)$$

where \mathbf{D}_j^i is the displacement of atom j at image i ($i = 1, \dots, N$). \mathbf{R}_j^1 and \mathbf{R}_j^N are the positions of atom j in the endpoint configurations. The power-law exponent α_j is a per-atom quantity that skews the displacement toward the beginning of the path ($\alpha_j < 1$) or toward the end ($\alpha_j > 1$). α

attains a minimum value α_{\min} at an arbitrarily chosen center ($r = 0$) and a maximum value α_{\max} at $r = L\sqrt{3}/2$, where L is the simulation-box length. This distance equals half the body diagonal and is the maximum minimum-image distance in a cubic periodic cell. For $r \in [0, L\sqrt{3}/2]$, α varies linearly as

$$\alpha = \alpha_{\min} + (\alpha_{\max} - \alpha_{\min}) \frac{2r}{L\sqrt{3}}. \quad (2)$$

Figure 1c summarizes how the per-atom interpolation profile depends on the exponent α . For the avalanche analyzed here, we choose $\alpha_{\min} = 0.1$ and $\alpha_{\max} = 10$. Using this scheme, we construct three distinct initial paths by centering the interpolation ($r = 0$) on each of the bonds involved in the avalanche. An NEB calculation is then performed for each path using the damped-dynamics optimizer quickmin [6], with convergence declared when the 2-norm of the global force vector falls below 10^{-4} eV Å⁻¹.

In Fig. 1d, we present the MEPs obtained by biasing the initial images toward the blue bond. The dotted black MEP (at $\gamma - \gamma_c = -0.03$) consists of a sequence of distinct energy minima separated by finite barriers. Each transition between consecutive minima corresponds to the breaking of a single bond, which is highlighted along the transition segments of the MEP. As the critical strain is approached, some barriers vanish; however, the bonds undergoing transformation remain well separated along the path. Biasing the initial images toward the orange or green bond leads to convergence onto the same final MEPs, in which the avalanche is initiated by breaking the orange bond, as shown in Fig. 1e. For the particular avalanche considered here, we do not observe any converged MEP in which the green bond acts as the initiating event. Nevertheless, for each investigated strain offset, the NEB calculations converge to two distinct MEPs depending on the initialization, indicating that multiple competing pathways exist and that the converged MEP is initialization-dependent. One could, in principle, continue approaching the critical strain and determine the physically relevant pathway by identifying which barrier drops to zero first. However, sufficiently close to the instability, the barriers become very shallow, approaching saddle points, and NEB calculations no longer converge in a robust manner.

[1] D. L. Malandro and D. J. Lacks, *J. Chem. Phys.* **110**, 4593 (1999).
[2] C. E. Maloney and A. Lemaître, *Phys. Rev. E* **74**, 016118 (2006).

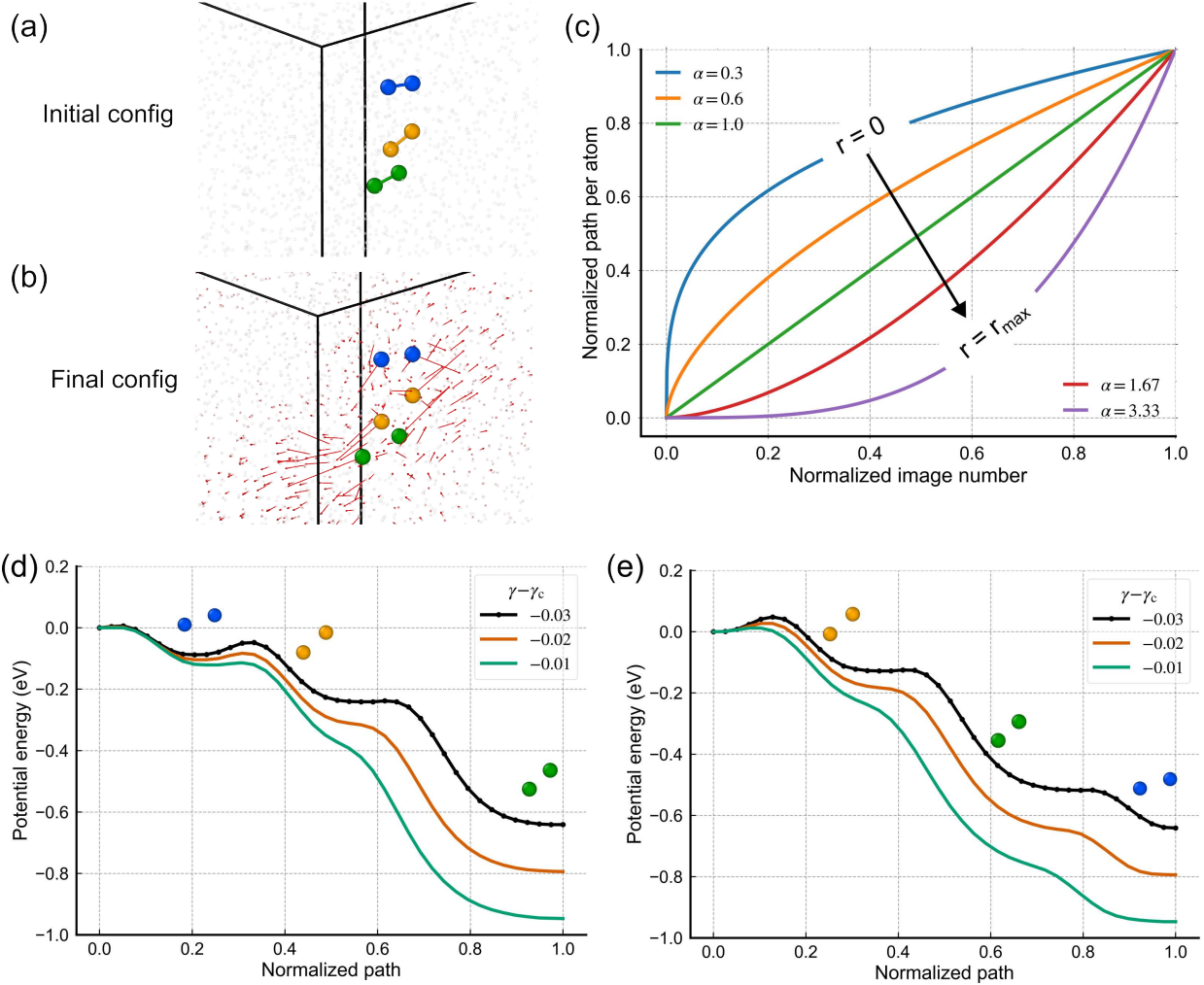


FIG. 1. Dependence of the MEP on the initial path. (a,b) Initial and final configurations bracketing the avalanche at an offset of $\gamma - \gamma_c = -0.03$. Atoms participating in the avalanche are highlighted in distinct colors, while all other atoms, which respond elastically, are rendered small and semi-transparent for clarity. The displacement field (red arrows) between the initial and final configurations is overlaid on panel (b). (c) Per-atom interpolation used to construct the initial images between the NEB endpoints: a power-law progression with exponent α that depends on the atom's distance r from an arbitrarily chosen center ($r = 0$). (d) MEPs obtained from NEB calculations with the initial images biased toward the blue bond at different values of strain offset $\gamma - \gamma_c$. (e) MEPs obtained when the initial images are biased toward the orange or green bond; both initializations converge to the same final paths. In both (d) and (e), atoms undergoing a plastic transformation are placed at their corresponding locations along the transition segments of the MEP.

- [3] G. Henkelman and H. Jónsson, *J. Chem. Phys.* **113**, 9978 (2000).
- [4] G. Henkelman, B. P. Uberuaga, and H. Jónsson, *J. Chem. Phys.* **113**, 9901 (2000).
- [5] F. Boioli, T. Albaret, and D. Rodney, *Phys. Rev. E* **95**, 033005 (2017).
- [6] D. Sheppard, R. Terrell, and G. Henkelman, *The Journal of Chemical Physics* **128**, 134106 (2008).

SUPPLEMENTARY MATERIAL B

TAILORED HESSIAN-FREE NUMERICAL CONTINUATION FOR ATOMISTIC MODELLING WITH MACHINE LEARNING INTERATOMIC POTENTIALS

B1 Periodic MLIP energy without restricting positions to the simulation cell

Let $A \in \mathbb{R}^{3 \times 3}$ be a matrix specifying a simulation cell $\Omega(A) := \{A\xi : 0 \leq \xi_i < 1\}$. Further, let $\mathcal{L}(A) = \{A\mathbf{n} : \mathbf{n} \in \mathbb{Z}^3\}$ denote the Bravais lattice spawned by A . Denote the atomic coordinates of the N atoms being modelled by

$$\mathbf{R} = (\mathbf{r}_1, \dots, \mathbf{r}_N) \in \mathbb{R}^{3N},$$

where, to make the computation of tangents in the numerical continuation scheme intuitive, *each* \mathbf{r}_i is allowed to be any point in \mathbb{R}^3 , i.e. we do *not* impose $\mathbf{r}_i \in \Omega(A)$.

Fix a finite interaction cutoff $r_c > 0$. Define the *neighbour-image set* of the i th atom by

$$\mathcal{N}_i(\mathbf{R}, A) := \{(j, \mathbf{n}) \in \{1, \dots, N\} \times \mathbb{Z}^3 : \|\mathbf{r}_j + A\mathbf{n} - \mathbf{r}_i\| < r_c\}.$$

Each element (j, \mathbf{n}) denotes the image of the j th atom translated by $A\mathbf{n}$. Form the multiset of relative vectors

$$\mathcal{R}_i(\mathbf{R}, A) := \{ \mathbf{r}_j + A\mathbf{n} - \mathbf{r}_i : (j, \mathbf{n}) \in \mathcal{N}_i(\mathbf{r}, A) \}.$$

Let \mathcal{E}_i be a general site energy mapping a finite multiset of relative vectors to \mathbb{R} (thus encompassing general many-body descriptors in MLIPs). Then define the periodic energy

$$\mathcal{E} : \mathbb{R}^{3N} \times \mathbb{R} \rightarrow \mathbb{R}, \quad \mathcal{E}(\mathbf{R}, \lambda) = \sum_{i=1}^N \mathcal{E}_i(\mathcal{R}_i(\mathbf{r}, A_\lambda)), \quad (1)$$

where $A_\lambda := T_\lambda A_0$, with A_0 the matrix defining the default simulation cell and T_λ a deformation gradient corresponding to a simple shear $\lambda = \varepsilon_{xy}$. To be precise,

$$T_\lambda = \begin{pmatrix} 1 & \lambda & 0 \\ 0 & 1 & 0 \\ 0 & 0 & 1 \end{pmatrix}.$$

The forces acting on the N atoms are defined as

$$\mathbf{F} : \mathbb{R}^{3N} \times \mathbb{R} \rightarrow \mathbb{R}^{3N}, \quad \mathbf{F}(\mathbf{R}, \lambda) := \nabla_{\mathbf{R}} \mathcal{E}(\mathbf{R}, \lambda).$$

B2 Hessian-free numerical continuation for MLIP systems

Numerical continuation is a set of tools to trace continuous paths of the form

$$\{(\mathbf{R}(s), \lambda(s)) \in \mathbb{R}^{3N+1} \mid s \in (0, 1), \quad \mathbf{F}(\mathbf{R}(s), \lambda(s)) = \mathbf{0}\}. \quad (2)$$

For a sufficiently locally smooth atomistic energy \mathcal{E} of the form given by (1), the existence of such a path of equilibrium configurations in the vicinity of an already known pair $(\mathbf{R}_k, \lambda_k)$ is guaranteed by the Implicit Function Theorem [1]. The parameter s is interpreted as arclength along the curve.

To find a nearby pair on the path (2), one first computes the tangent vector

$$(\dot{\mathbf{R}}_k, \dot{\lambda}_k) := \frac{d}{ds}(\mathbf{R}_k(s), \lambda_k(s)), \quad (3)$$

and then solves an extended system of equations $\mathbf{G}(\mathbf{R}_{k+1}, \lambda_{k+1}) = 0$, where

$$\mathbf{G} : \mathbb{R}^{3N+1} \rightarrow \mathbb{R}^{3N+1}, \quad \mathbf{G}(\mathbf{R}, \lambda) := \begin{pmatrix} \mathbf{F}(\mathbf{R}, \lambda) \\ (\mathbf{R} - \mathbf{R}_k)^\top \dot{\mathbf{R}}_k + (\lambda - \lambda_k) \dot{\lambda}_k - \delta s \end{pmatrix}, \quad (4)$$

starting from the initial guess $(\mathbf{R}_k + \delta s \dot{\mathbf{R}}_k, \lambda_k + \delta s \dot{\lambda}_k)$. It is well known [1] that this extended system remains regular even at points where the Jacobian of \mathbf{F} , denoted $\nabla_{\mathbf{R}} \mathbf{F}$ (the Hessian of the atomistic energy $\nabla_{\mathbf{R}}^2 \mathcal{E}$), is singular. Moreover, for sufficiently small $\delta s > 0$, it can be rigorously shown that the new solution $(\mathbf{R}_{k+1}, \lambda_{k+1})$ remains on the same path (2) [1].

The robustness of the method relies on accurate tangent computation. In principle, the tangent (3) is obtained by differentiating the condition in (2) with respect to s , which requires access to $\nabla_{\mathbf{R}} \mathbf{F} = \nabla_{\mathbf{R}}^2 \mathcal{E}$. This is prohibitively expensive for modern MLIPs, so we instead approximate the tangent using finite differences between previous solutions. Similarly, to avoid computing the full Hessian when solving (4), we use a Krylov-subspace approach, which only requires the ability to compute matrix-vector products with $\partial_{\mathbf{R}} \mathbf{F}$, which themselves can be approximated by finite differences. Related ideas have recently been explored in [2]. Our continuation code, LACT [3] is a Python-based wrapper around the molecular dynamics code LAMMPS [4].

B3 Ensuring relevance of computed paths

The energy landscape associated with \mathcal{E} is highly complex, and not every continuation path of the form (2) obtained with base continuation routine described in A2 is physically relevant. To isolate the meaningful branches, we employ the automated procedure detailed in Algorithm 1. The energy plots shown in the main text are based directly on outputs of this scheme.

B4 Overcoming numerical stability issues with traversing bifurcation points

In practice, some bifurcation points involve such a sharp turn with respect to λ that a minuscule δs is required to traverse it. This in turn leads to numerical stability issues when computing tangents with finite difference approximations, often leading to a solution path artificially turning on itself. To avoid this, close to a bifurcation point, we switch to a force-based continuation scheme detailed in Algorithm 2.

- [1] E. L. Allgower and K. Georg, *Introduction to numerical continuation methods* (SIAM, 2003).
- [2] I. Maliov, P. Grigorev, and T. D. Swinburne, npj Comput. Mater. **11**, 22 (2025).
- [3] M. Buze and F. Birks, LACT (LAMMPS Continuation Techniques), <https://github.com/mbuze/LACT>.
- [4] A. P. Thompson, H. M. Aktulga, R. Berger, D. S. Bolintineanu, W. M. Brown, P. S. Crozier, P. J. in 't Veld, A. Kohlmeyer, S. G. Moore, T. D. Nguyen, R. Shan, M. J. Stevens, J. Tranchida, C. Trott, and S. J. Plimpton, Comput. Phys. Commun. **271**, 108171 (2022).

Algorithm 1: Recursive continuation with avalanche dissection

Input: Initial minimum \mathbf{R}_0 at parameter λ_0

Output: Set of physically relevant continuation paths

Stage 1: Accelerated quasi-static loading

Run continuation algorithm until increment $\Delta\lambda$ changes sign (bifurcation point).

Perform quasi-static loading to trigger avalanche; record bonds involved

Stage 2: Saddle-point tracing

Use Algorithm 2 to traverse sharp bifurcation point onto the saddle.

Restart continuation and run on saddle until $\Delta\lambda$ changes sign.

Stage 3: Restart or termination

for a uniformly sampled subset of saddle points (\mathbf{R}, λ) : **do**

 Take current saddle \mathbf{R}_k and relax, obtaining local minima \mathbf{R}_k^0 . Perturb \mathbf{R}_k by $\delta \frac{\mathbf{R}_k - \mathbf{R}_k^0}{|\mathbf{R}_k - \mathbf{R}_k^0|}$ and
 relax again, obtaining a second local minima \mathbf{R}_k^1 .

foreach newly identified minima pair **do**

if the structural change between them only involves a previously unexplored subset of avalanche
 bonds **then**
 Record as a candidate restart position.

else

 Disregard as irrelevant.

foreach candidate restart position **do**

if candidate has highest λ in a chain of at least two candidate restarts which each have the same
 subset of avalanche bonds **then**
 Keep candidate

else

 Discard candidate

if At least one candidate position remaining **then**

if If only remaining candidate involves all remaining bonds in the avalanche **then**
 Terminate, marking avalanche as successfully explored.

else

 Restart algorithm from the highest λ candidate showing the smallest subset of avalanche
 bonds.

else

 Terminate, marking avalanche as not fully explored.

Algorithm 2: Force-assisted continuation through bifurcation points

Input: Initial minimum \mathbf{R}_0 at parameter λ_0

Output: Set of physically relevant continuation paths

Stage 1: Accelerated quasi-static loading

Run continuation until the increment $\Delta\lambda$ changes sign (bifurcation point).

Step back and perform quasi-static loading to trigger avalanche; record the set of bonds $\{(\mathbf{r}_i, \mathbf{r}_j)\}$ involved.

Stage 2: Force-based continuation

Roll back five continuation steps. Among avalanche bonds, select $(\mathbf{r}_i, \mathbf{r}_j)$ with the largest $\frac{d}{d\lambda}|\mathbf{r}_i - \mathbf{r}_j|$ (approximated by finite differences).

Freeze λ and define an auxiliary force field $\mathbf{F}^\mu(\mathbf{R}) = (\mathbf{f}_1^\mu, \dots, \mathbf{f}_N^\mu)$ with

$$\mathbf{f}_i^\mu = \mu \frac{\mathbf{r}_i - \mathbf{r}_j}{|\mathbf{r}_i - \mathbf{r}_j|}, \quad \mathbf{f}_j^\mu = -\mathbf{f}_i^\mu, \quad \mathbf{f}_k^\mu = 0 \quad (k \neq i, j),$$

where \mathbf{F}^μ depends on current configuration \mathbf{R} .

Initialise with $\mu = 0$ and run continuation as in (A2), replacing \mathbf{F} by $\mathbf{F} + \mathbf{F}^\mu$ and treating μ as the continuation parameter.

Stage 3: Return to standard continuation

Terminate the force-based routine once $\Delta\mu$ changes sign and subsequently μ returns to zero. The corresponding configuration is guaranteed to be a saddle point.

SUPPLEMENTARY MATERIAL C
SEPARABILITY OF AVALANCHES

I. INVESTIGATING SEPARABILITY

A central issue in the study of avalanches in amorphous carbon is their separability – that is, the extent to which they can be decomposed into transitions between intermediate basins occurring at strains below the avalanche onset. To investigate this, we applied our numerical continuation algorithm to explore the energy landscapes of the first 51 plastic events across three different 4096 atom amorphous carbon systems (a total of 153 events). For each event, we recorded (i) the number of bonds involved in the avalanche and (ii) the ‘degree of separability’ (how many intermediate states we could recover at lower strains).

This information is displayed for all events successfully explored in Fig. 1. The distribution of the number of bonds involved in plastic events is shown in Fig. 1a. It can be seen that the majority of plastic events involve only a single bond, with larger plastic events becoming increasingly less common. The separability of plastic events is shown as a scatter plot in Fig. 1b. The dashed line represents ‘perfect separability’ – a perfectly separable avalanche involving N bonds can be split into N discrete transitions at strains below the onset. We found that the majority of plastic events involving multiple bonds were separable to some extent, but relatively few were perfectly separable.

We found three common explanations for this. First, it was common for the same atom to be involved in the breaking of one bond and the forming of another during a single plastic event. Our criteria classified such an event as involving two bonds, but energetically this transition behaves like an inseparable single-bond event. Second, on occasion, the bond detection algorithm mistakenly classified a bond as breaking or forming during an avalanche when in reality it only stretched or compressed slightly - erroneously inflating the number of bonds involved. Finally (and most commonly), the single bond events were so correlated that they could not be disentangled at lower strains.

It is important to make a distinction between the highly correlated chains of single-bond events seen here and the collective motion of many atoms (like one sees, for example, in Lennard-Jones

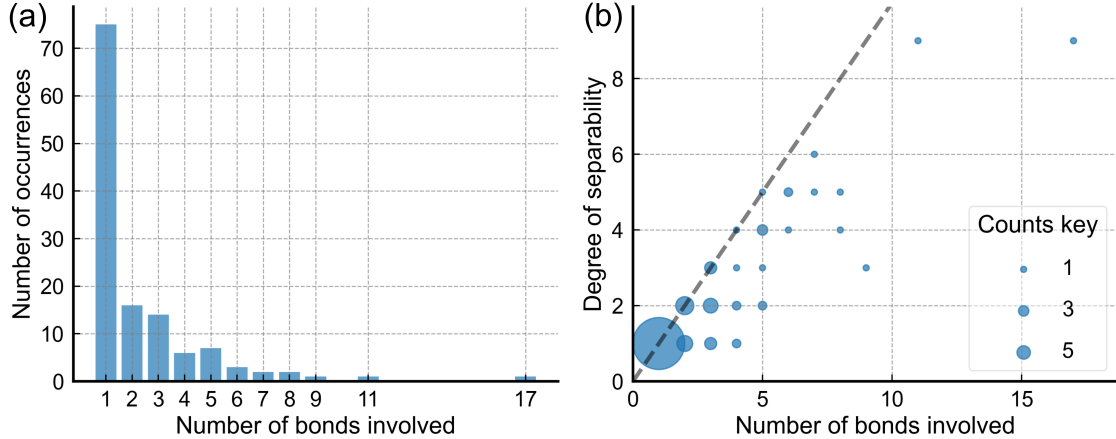


FIG. 1. A demonstration of the size and separability of the first 51 plastic events across three amorphous carbon structures that were successfully explored by the algorithm. (a) The occurrence of events by number of bonds. More than half of the events involve just one bond. (b) Degree of separability of different plastic events. The majority of events involving multiple bonds are at least partially separable. The dashed line represents ‘perfect separability’, with points on that line corresponding to avalanches that have been perfectly separated into chains of single bond events.

metallic glass systems). Crucially, in amorphous carbon, even in the case of an inseparable correlated chain of single bond events, the initial saddle point is index-1 and involves only a single bond.

II. METHOD LIMITATIONS AND IMPROVEMENTS

Of the 153 events analyzed, there were 25 instances where the algorithm failed during the exploration of an avalanche. The statistics of these failures can be seen in Fig. 2. For the most part, these failures can be attributed to the slight unpredictability of the relaxation stage of the algorithm (where relaxations are initiated from uniformly sampled saddle points on an unstable branch). For the algorithm to perform perfectly, it is essential that single-bond events only trigger if they have a barrier of zero. However, in practice, when there are many small barriers in the system (as is common in the plastic flow regime), it is common for small (\sim meV) barriers to be overcome during a relaxation. If this happens, neighboring local minima can involve very different subsets of bonds in the full avalanche causing the exploration to fail.

One possible way of overcoming this would be to replace the relaxation with a continuation using

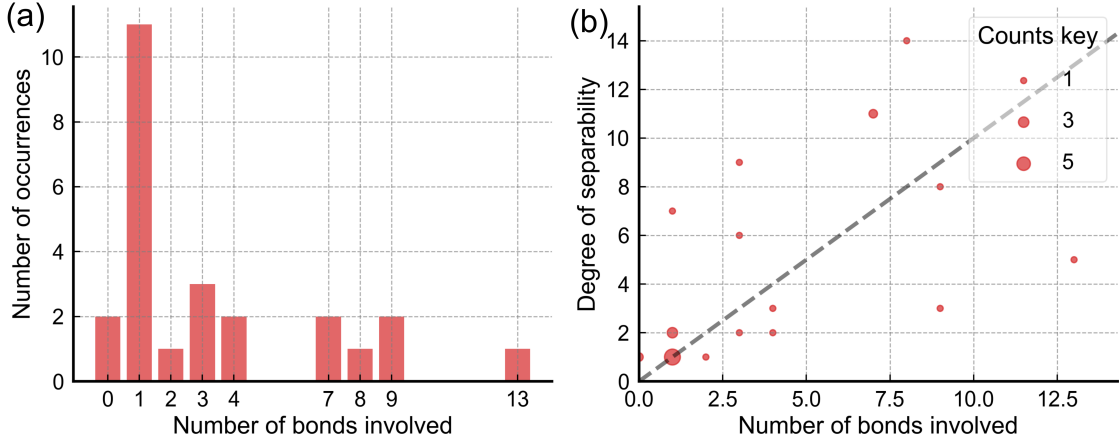


FIG. 2. A demonstration of the size and separability of the first 51 plastic events across three amorphous carbon structures that the algorithm failed to correctly explore. (a) The occurrence of events by number of bonds. Note that the the algorithm disproportionately fails on larger avalanches in the plastic flow regime. (b) Degree of separability of different plastic events. Many events are 'more than perfectly separable', indicating that other bonds broke during the exploration which were not part of the initial avalanche. Most failures are due to the relaxation algorithm overcoming small barriers to trigger events that were not part of the initial avalanche.

a more suitable (and localized) continuation coordinate than the strain on the system. Selecting such a coordinate for the case of a single-bond is simple – one can just use a force applied to the bond (as is done in Algorithm 2 in Supplementary Material B). Selecting a suitable coordinate for multi-bond avalanches however is a non-trivial endeavor, and is therefore left as an interesting direction for future work.

SUPPLEMENTARY MATERIAL D

CAUSALITY CHAIN OF EVENTS IN AVALANCHES

Our analysis in the main manuscript demonstrates that plastic avalanches in a-C networks possess a *latent internal structure*, manifested as a hierarchy of energy barriers revealed by numerical continuation, each associated with the transformation of an individual bond. This hierarchy naturally introduces a notion of causality within a single avalanche, whereby the activation of one bond-level instability facilitates subsequent transformations. To explicitly probe this causal sequence, we study the real-time dynamical evolution of avalanches. The system dynamics are modeled using overdamped equations of motion, appropriate for the strongly dissipative, athermal regime relevant to quasi-static deformation. The atomic positions $\mathbf{r}(t)$ evolve according to

$$\dot{\mathbf{r}}(t) = \frac{1}{\zeta} \mathbf{F}(\mathbf{r}(t), t) , \quad (1)$$

where \mathbf{F} denotes the total interatomic force and ζ is the damping coefficient controlling the relaxation rate. Equation (1) is integrated numerically using the Heun method [1], a second-order explicit predictor–corrector scheme:

$$\begin{aligned} \text{(predictor)} \quad \tilde{\mathbf{r}}_{n+1} &= \mathbf{r}_n + \frac{\Delta t}{\zeta} \mathbf{F}(\mathbf{r}_n) , \\ \text{(corrector)} \quad \mathbf{r}_{n+1} &= \mathbf{r}_n + \frac{\Delta t}{2\zeta} [\mathbf{F}(\mathbf{r}_n) + \mathbf{F}(\tilde{\mathbf{r}}_{n+1})] . \end{aligned} \quad (2)$$

where Δt denotes the integration timestep. To initiate an avalanche, the system is first driven arbitrarily close to the critical strain at which the instability occurs. A small additional shear strain increment of $\Delta\gamma = 10^{-5}$ is then applied to trigger the event. Following this perturbation, the system is allowed to evolve dynamically according to Eq. (2) with a damping coefficient $\zeta = 0.2 \text{ eV} \cdot \text{ps} \cdot \text{\AA}^{-2}$ and a timestep $\Delta t = 10^{-4} \text{ ps}$.

The results are summarized in Figs. 1 and 2, corresponding to a small avalanche involving three bond transformations and a larger avalanche comprising six transformations, respectively. In both figures, panel (a) shows the sequence of events obtained from numerical continuation, where the hierarchy of bond-level instabilities is ordered from bottom to top. Panel (b) presents the corresponding results from the overdamped dynamical simulations. The vertical axis reports a bond-level activity measure given by the normalized change in bond length between the initial and

post-avalanche final configurations. The color coding is identical in panels (a) and (b), facilitating direct comparison between both methods. The sequence of events observed in the small avalanche shown in Fig. 1b follows the same hierarchy predicted by numerical continuation in Fig. 1a. In contrast, for the larger avalanche (Fig. 2), the agreement between the two approaches holds only for the first four bond transformations; beyond this point, it breaks down, with the ordering of the final two events reversed.

While both approaches capture the overall structure of bond-level avalanches, the difference observed in the larger avalanche naturally raises the question of which description should be adopted as a reference when resolving the detailed ordering of individual bond transformations. From our perspective, numerical continuation provides the more faithful representation, as it follows the system along the underlying potential energy landscape and directly identifies the sequence of stability losses associated with successive bond transformations. By contrast, overdamped dynamics advances the system through explicit time integration, whose outcome may be influenced by finite time stepping, numerical noise, and the dynamical competition between closely spaced instabilities. Such effects may obscure the fine ordering of individual events, particularly at later stages of an avalanche.

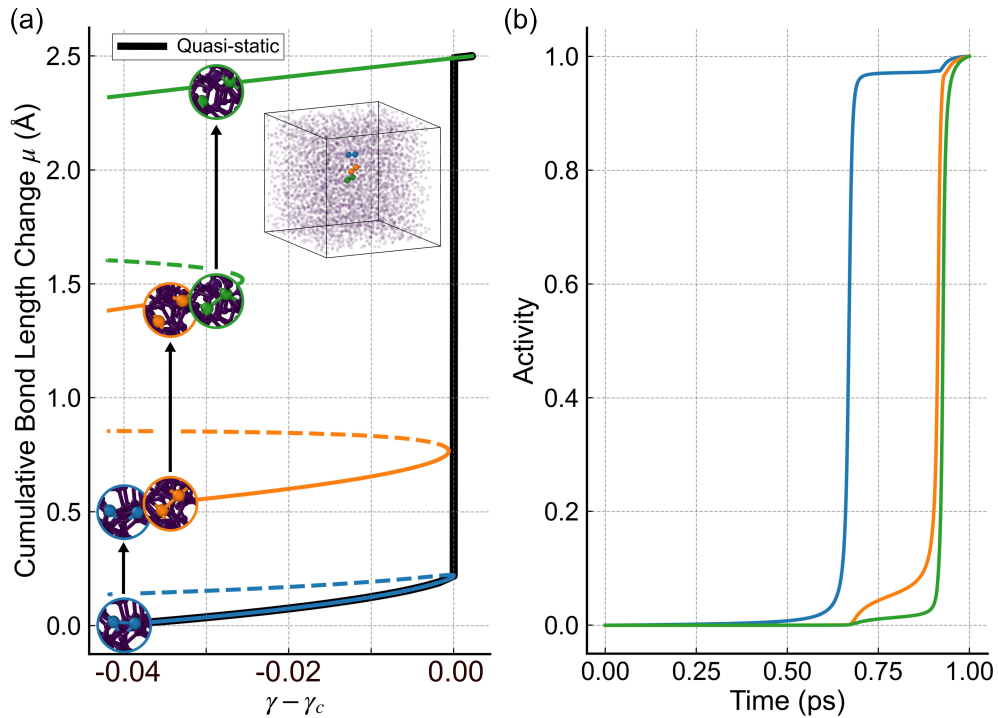


FIG. 1. Chain of events within an avalanche involving three bond transformations. (a) Hierarchy of bond-level instabilities obtained from numerical continuation, ordered from bottom to top. (b) Corresponding overdamped dynamical evolution of the same bonds during the avalanche. Colors are consistent between panels.

[1] F. Sammüller and M. Schmidt, The Journal of Chemical Physics **155**, 134107 (2021).

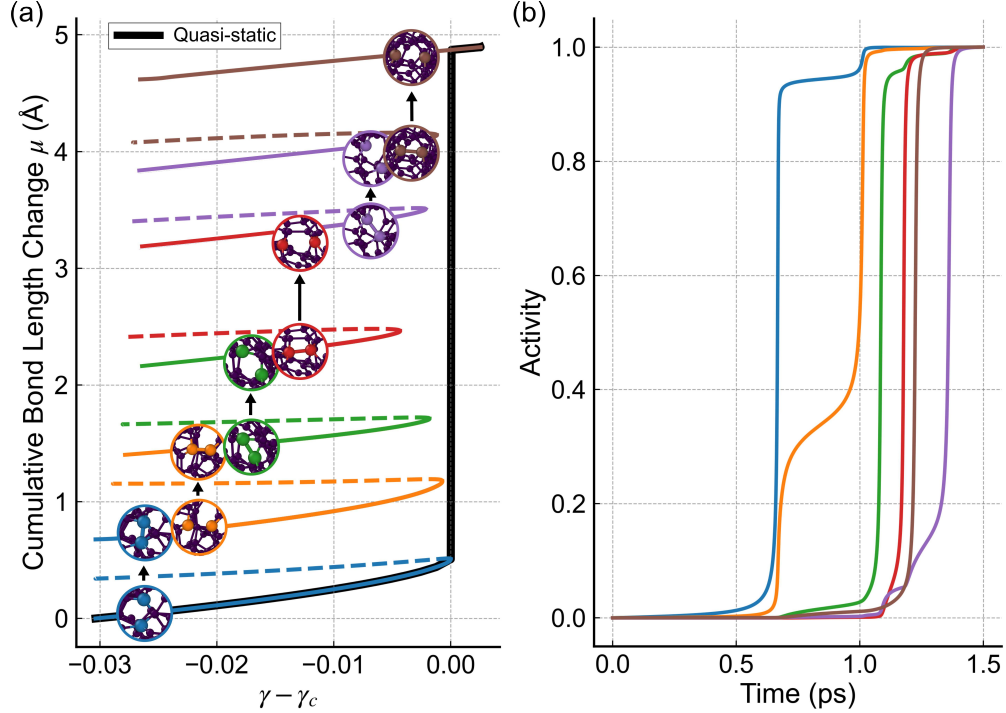


FIG. 2. Chain of events within an avalanche involving six bond transformations. (a) Hierarchy of bond-level instabilities obtained from numerical continuation, ordered from bottom to top. (b) Corresponding overdamped dynamical evolution of the same bonds during the avalanche. Colors are consistent between panels.